Journal of Solid State Chemistry 183 (2010) 1935–1942

Contents lists available at ScienceDirect

Journal of Solid State Chemistry

journal homepage: www.elsevier.com/locate/jssc

Crystal growth and properties of $Ln_2Ag_{1-x}Ga_{10-y}$ (Ln=La, Ce), a disordered variant of the Ce_2NiGa_{10}-structure type

Melissa C. Menard [a], Yimin Xiong [b], Amar B. Karki [b], Brenton L. Drake [a], Philip W. Adams [b], Frank R. Fronczek [a], David P. Young [b], Julia Y. Chan [a,*]

[a] Department of Chemistry, Louisiana State University, 232 Choppin Hall, Baton Rouge, LA 70803-1804, USA
[b] Department of Physics and Astronomy, Louisiana State University, 202 Nicholson Hall, Baton Rouge, LA 70803-1804, USA

ARTICLE INFO

Article history:
Received 8 March 2010
Received in revised form
11 June 2010
Accepted 21 June 2010
Available online 25 June 2010

Keywords:
Cerium
Gallium
Crystal growth
Magnetic properties

ABSTRACT

We report the flux growth and characterization of $Ln_2Ag_{1-x}Ga_{10-y}$ (Ln=La, Ce), a disordered variant of the Ce_2NiGa_{10} structure type. Single crystals of $La_2Ag_{1-x}Ga_{10-y}$ ($x\sim0.3$; $y\sim0.6$) and $Ce_2Ag_{1-x}Ga_{10-y}$ ($x\sim0.3$; $y\sim0.9$) were grown by the self-flux method and characterized using single-crystal X-ray diffraction. Transport measurements of $Ce_2Ag_{1-x}Ga_{10-y}$ ($x\sim0.3$; $y\sim0.9$) reveal metallic behavior with a transition at 3 K. Magnetic measurements indicate antiferromagnetic ordering at 3 K of localized Ce^{3+} moments for $Ce_2Ag_{1-x}Ga_{10-y}$. Magnetoresistance is positive with a maximum value of 16% at 9 T. $La_2Ag_{1-x}Ga_{10-y}$ exhibits metallic behavior with magnetic susceptibility showing temperature independent paramagnetism. We will compare $Ce_2Ag_{1-x}Ga_{10-y}$ ($x\sim0.3$; $y\sim0.9$) to Ce_2NiGa_{10} to examine the effects of transition metal substitution and to the related $Ce(Ag,Ga)_4$ phase to examine the effects of crystal structure on the physical properties.

1. Introduction

Complex Ga-networks have been a popular subject due to the observation of a wide variety of exotic phenomena found in these systems: superconductivity in $PuCoGa_5$ [1–3], large magnetoresistance in Ln_4PtGa_{12} (Ln=Dy–Er) [4], heavy fermion behavior in $CePdGa_6$ [5], charge density wave formation in $LnCo_xGa_3Ge$ (Ln=Y, Gd) [6,7], spin density wave formation in $U_3Ga_2Si_3$ [8], the observation of zero thermal expansion of YbGaGe [9], and negative thermal expansion of $YbGa_{1+x}Ge_x$ [10]. Identification of structural subunits associated with specific phenomena serves as a guide to focus crystal growth on targeted motifs in new materials likely to yield a desired property. In all cases novel materials and behaviors, with targeted motifs, are expected due to differing coordination preferences, electronegativities, atomic sizes, and disorder in new materials among transition metals.

We have recently grown and characterized single crystals of several ternary phases of Ce–M–Ga (M=Ni, Pd, Cu) and discovered unusual magnetic and electrical properties [5,11–16]. $CePdGa_6$ is a heavy fermion antiferromagnet ($\gamma\sim400$ mJ/molK^2) [5] with a layered structure of alternating face-sharing $CeGa_{8/4}$ rectangular prisms and staggered edge-sharing Pd rectangular prismatic layers, and is structurally similar to the magnetically mediated superconductors $CeMIn_5$ (M=Co, Rh, Ir) [17–19]. The structural similarity of $CePdGa_6$ to the magnetically mediated superconductors $CeMIn_5$ (M=Co, Rh, Ir) [17–19] has driven the continued investigation of ternary systems of Ln:M:Ga (Ln=lanthanide, M=transition metal) to make connections between structural motifs and unique physical properties. Subsequent investigation resulted in the growth of antiferromagnetic Ce_2PdGa_{12}, which is an intergrowth of $CePdGa_6$- and CaF_2-type structure segments, with Ce and Pd in rectangular prismatic environments and shows moderate heavy fermion behavior [12]. A related phase, Ce_2PdGa_{10}, is paramagnetic down to 2 K, shows large magnetoresistance of 290% at 9 T, and can be described as an intergrowth of $BaAl_4$- and CaF_2-type structure segments [11]. A copper analogue, Ce_2CuGa_{12} [13], exhibits large magnetoresistance up to 65% at 9 T. The isostructural Ni-analogue, Ce_2NiGa_{12}, orders antiferromagnetically at 10 K and undergoes a metamagnetic transition at 3 T [13].

Transition metal substitution led to the investigation of Ag-containing intermetallic compounds. Although the structure of several Ln:Ag:Ga (Ln=lanthanide) intermetallic compounds such as $Ln(Ag,Ga)_4$ (Ln=La–Nd, Sm, Yb) [20,21], $Ln_3(Ag,Ga)_{11}$ (Ln=Y, Gd–Yb) [22,23], $LnAgGa_2$ (Ln=Gd, Yb, Y) [23–25], $LnAgGa$ (Ln=Tb– Ho)[26], $Ln(Ag,Ga)_2$ (Ln=La–Nd, Sm–Lu, Y) [23,27,28], $Ln_5(Ag,Ga)_{19-x}$ (Ln=Gd, Tb; $x\sim2.2$) [29], $CeAg_{4.12}Ga_{6.88}$ [30], $CeAg_{1.25}Ga_{4.25}$ [30], $Gd_{14}(Ag,Ga)_{51}$ [25], Gd(Ag,Ga) [25], and $Ln(Ag,Ga)_3$ (Ln=Sm, Gd, Tb–Tm, Lu) [31] have been reported, the structure determination of most are from polycrystalline samples and the physical properties of most of these compounds have not been investigated. Here we report the flux growth and

* Corresponding author.
E-mail address: jchan@lsu.edu (J.Y. Chan).

0022-4596/$ - see front matter © 2010 Elsevier Inc. All rights reserved.
doi:10.1016/j.jssc.2010.06.011

characterization of $Ln_2Ag_{1-x}Ga_{10-y}$ (Ln=La, Ce), a disordered variant of the Ce_2NiGa_{10} structure-type [32]. We will compare $Ce_2Ag_{1-x}Ga_{10-y}$ ($x\sim0.3$; $y\sim0.9$) to Ce_2NiGa_{10} to examine the structural changes with transition metal substitution and to the structurally related Ce(Ag,Ga)$_4$ [14,20,33,34] ($BaAl_4$-structure type) to examine the effects of crystal structure on the physical properties.

2. Synthesis

Single crystals of $La_2Ag_{1-x}Ga_{10-y}$ ($x\sim0.3$; $y\sim0.6$) and $Ce_2Ag_{1-x}Ga_{10-y}$ ($x\sim0.3$; $y\sim0.9$) were grown by the self-flux method. La or Ce rod (3 N), Ag powder (3 N), and Ga pellets (6 N) were used as-received, placed in an alumina crucible in a mole ratio of 2:1:20, and sealed in evacuated fused silica tubes.

2.1. Reaction profile

The reaction profile involved heating the reaction ampoule to 1150 °C at a rate of 200 °C/h. After dwelling for 12 h, the tube was cooled to 500 °C at 200 °C/h and then cooled to 400 °C at 2 °C/h. After dwelling at 400 °C for 5 days, the tube was inverted and spun to remove excess flux. Hot water and dilute HCl were used to remove excess Ga from the surface of the crystals. Crystals grew as layered aggregates ($0.5\times10\times10$ mm^3) with typical single crystal size of approximately $0.025\times0.5\times0.5$ mm^3 and a typical yield of 80%. The crystals showed no noticeable oxidation in air. $Ln_2Ag_{1-x}Ga_{10-y}$ (Ln=La and Ce) were grown in several batches using the above described reaction profile. The cooling rate of 2 °C/h appears to be a determining factor in the growth of $Ln_2Ag_{1-x}Ga_{10-y}$ (Ln=La, Ce). Other two step cooling sequences used included a fast cool rate of 200 °C/h to 500 °C then a slow cool rate 8 °C/h (or 4 °C/h) to 400 °C followed by dwelling for 5 days. One-step fast cooling sequences used included cooling at a rate of 200 °C/h to 400 °C and cooling at a rate of 200 °C/h to 650 K. These sequences resulted in the growth of Ce(Ag,Ga)$_4$ ($BaAl_4$-structure type). Systematic investigation of the reaction profile through adjustments of the dwell time at the highest dwelling temperature (1150 °C), the cooling rate of the fast step (200 °C/h), the cooling rate of the slow step (2 °C/h), the spin temperature (400 °C), or the final dwell time (5 days) led to the formation of phases of the $BaAl_4$-structure type except for the first reaction profile given above. Annealing of $Ln_2Ag_{1-x}Ga_{10-y}$ (Ln=La, Ce) crystals at 650 °C (or 400 °C) for several hours to several days resulted in the growth of Ce(Ag,Ga)$_4$ ($BaAl_4$-structure type).

2.2. Homogeneity range

Systematic investigation of the reaction ratio was carried out to establish a homogeneity range by varying the composition of each reactant separately. This compound exhibits a very narrow phase width, consistent with the composition of energy-dispersive X-ray spectroscopy (EDXS) ($La_2Ag_{0.67(5)}Ga_{9.17(13)}$ and $Ce_2Ag_{0.67(9)}Ga_{9.25(8)}$) and with the composition of single crystal X-ray diffraction ($La_2Ag_{0.7(1)}Ga_{9.4(1)}$ and $Ce_2Ag_{0.7(1)}Ga_{9.1(1)}$).

3. Experimental

3.1. Single crystal and powder X-ray diffraction

Ground aggregates of $Ln_2Ag_{1-x}Ga_{10-y}$ (Ln=La, Ce) were characterized by X-ray powder diffraction using a Bruker AXS D8 Advance diffractometer with Cu $K\alpha$ radiation (λ=1.5418 Å) to ensure phase purity of each batch and the diffraction patterns are consistent with the refined model. Silver-colored fragments of single crystals of $La_2Ag_{1-x}Ga_{10-y}$ ($x\sim0.3$; $y\sim0.6$) and

Table 1
Crystallographic data (tetragonal, $I4/mmm$).

Crystal data				
Composition	$La_2Ag_{0.7(1)}Ga_{9.4(1)}$	$La_2Ag_{0.7(1)}Ga_{9.4(1)}$	$Ce_2Ag_{0.7(1)}Ga_{9.1(1)}$	$Ce_2Ag_{0.7(1)}Ga_{9.1(1)}$
a (Å)	4.3381(6)	4.3236(6)	4.2928(6)	4.2769(6)
c (Å)	26.1630(18)	26.1020(18)	26.1240(15)	26.0750(15)
V (Å^3)	492.36(10)	487.94(10)	481.42(10)	476.96(10)
Z	2	2	2	2
Crystal size (mm^3)	$0.03\times0.05\times0.06$	$0.03\times0.05\times0.06$	$0.03\times0.03\times0.03$	$0.03\times0.03\times0.03$
Data collection				
Temperature (K)	298	100	298	100
Measured reflections	1069	708	6752	4104
Independent reflections	376	266	280	279
Reflections with $I>2\sigma(I)$	314	223	265	245
R_{int}	0.0331	0.0278	0.0252	0.0425
h	−6→6	−6→6	−4→6	−6→6
k	−4→6	−4→6	−6→6	−4→4
l	−41→42	−36→35	−37→37	−37→37
Refinement				
θ range (deg.)	1.56–34.95	1.56–30.01	3.12–30.86	4.69–30.96
[a]$R_1[F^2>2\sigma F^2)]$	0.0211	0.0339	0.0263	0.0279
[b]$wR_2(F^2)$	0.0453	0.0723	0.0497	0.0677
Parameters	25	20	25	20
GooF on F^2	1.432	1.937	1.110	1.154
μ (mm^{-1})	34.769	35.084	35.503	35.871
Δp_{max} (eÅ^{-3})	2.043	2.193	1.358	2.108
Δp_{min} (eÅ^{-3})	−1.327	−2.585	−1.183	−1.334
Extinction coefficient ($\times10^{-4}$)	46(4)	28(5)	26(2)	26(3)

[a] $R_1=\Sigma||F_0|-|F_c||/\Sigma|F_0|$.
[b] $wR_2=[\Sigma w(F_0^2-F_c^2)^2/\Sigma w(F_0^2)^2]^{1/2}$; $P=(F_0^2+2F_c^2)/3$; $w=1/[\sigma^2(F_0^2)+8.9P]$, $w=1/[\sigma^2(F_0^2)+(0.0114P)^2+8.9P]$, $w=1/[\sigma^2(F_0^2)+9.8P]$, and $w=1/[\sigma^2(F_0^2)+(0.0235P)^2+8.9P]$ for $La_2Ag_{0.7(1)}Ga_{9.4(1)}$ (298 K), $La_2Ag_{0.7(1)}Ga_{9.4(1)}$ (100 K), $Ce_2Ag_{0.7(1)}Ga_{9.1(1)}$ (298 K), $Ce_2Ag_{0.7(1)}Ga_{9.1(1)}$ (100 K), respectively.

$Ce_2Ag_{1-x}Ga_{10-y}$ ($x\sim0.3$; $y\sim0.9$) ($0.03\times0.05\times0.06$ and $0.03\times0.03\times0.03$ mm^3, respectively) were glued to glass fibers with epoxy and mounted on the goniometer of a Nonius Kappa CCD diffractometer equipped with Mo $K\alpha$ radiation ($\lambda=0.71703$ Å). High-resolution data were collected up to $\theta=31^\circ$ at 298 and 100 K for both analogues. SIR 92 [35] was used to obtain a starting model (Laue class 4/*mmm*), and SHELXL-97 [36] was used for structure refinement. The room temperature structures for $Ln_2Ag_{1-x}Ga_{10-y}$ (Ln=La, Ce) were refined anisotropically in space group *I*4/*mmm* (No. 139) with $R_1=0.0211$ and $R_1=0.0263$ for La and Ce at 298 K. The 100 K data for $Ln_2Ag_{1-x}Ga_{10-y}$ (Ln=La, Ce) were modeled with isotropic atomic displacement parameters for Ga2 and Ga6 and anisotropic displacement parameters were assigned for the remaining atomic positions. No missing symmetry elements were found for this solution using PLATON [37]. Further crystallographic parameters are provided in Table 1.

3.2. Refinement of structural disorder

Disorder is observed at the *M*1 (4*d*) (*M*=Ag+Ga), Ga2 (8*g*), Ga5 (2*b*), and Ga6 (16*n*) sites. Low temperature data collections were used to determine the nature of the disorder, static or dynamic. The nature of the disorder for both $La_2Ag_{1-x}Ga_{10-y}$ ($x\sim0.3$; $y\sim0.6$) and $Ce_2Ag_{1-x}Ga_{10-y}$ ($x\sim0.3$; $y\sim0.9$) is best described as static since both 100 and 298 K data collections yield the same structural model with no splitting of disordered sites in the 100 K data collection. There are two types of static disorder present in this phase: mixing of Ag and Ga at the *M*1 (4*d*) site (*M*1=Ag1+Ga1) and partial occupancy of Ga at the Ga2 (8*g*), Ga5 (2*b*), and Ga6 (16*n*) sites. The presence of large atomic displacement parameters, anomalies in the electron difference maps, and anomalous residual electron density are indications of disorder at the *M*1, Ga2, Ga5, and Ga6 sites. Mixing between Ag and Ga has been reported previously in AgGa-containing intermetallic compounds due to the similar size, electronegativity, and coordination preferences of Ag and Ga [20–25,27–31,38]. The occupancy and atomic displacement parameters of *M*1 (Ag1+Ga1), Ga2, Ga5, and Ga6 sites were first refined separately and then together to yield the occupancies shown in Table 2.

3.3. EDXS

The composition of aggregates ($0.5\times10\times10$ mm^3) of $Ln_2Ag_{1-x}Ga_{10-y}$ (Ln=La, Ce) were characterized with the energy-dispersive X-ray spectroscopy (EDXS) option of a JEOL JSM-5060 scanning electron microscope. The accelerating voltage was 15 kV

Table 2
Positional and atomic displacement parameters.

Atom	Wyckoff position	*x*	*y*	*z*	Occ.[a]	U_{eq} (Å^2)[b]
$La_2Ag_{0.7(1)}Ga_{9.4(1)}$						
298 K						
La	4*e*	0	0	0.35258(3)	1.00	0.0081(2)
*M*1	4*d*(0.31(2)Ag+0.69(2)Ga)	0	$\frac{1}{2}$	$\frac{1}{4}$	1.00	0.0103(3)
Ga2	8*g*	0	$\frac{1}{2}$	0.9520(4)	0.38(2)	0.022(3)
Ga3	4*e*	0	0	0.09907(5)	1.00	0.0112(3)
Ga4	4*e*	0	0	0.19412(5)	1.00	0.0101(3)
Ga5	2*b*	0	0	$\frac{1}{2}$	0.15(2)	0.026(4)
Ga6	16*n*	0	0.383(2)	0.4561(3)	0.29(3)	0.0238(18)
100 K						
La	4*e*	0	0	0.35263(5)	1.00	0.0051(4)
*M*1	4*d*(0.31(2)Ag+0.69(2)Ga)	0	$\frac{1}{2}$	$\frac{1}{4}$	1.00	0.0053(3)
Ga2	8*g*	0	$\frac{1}{2}$	0.9524(2)	0.38(2)	0.0061(9)
Ga3	4*e*	0	0	0.09888(9)	1.00	0.0063 (6)
Ga4	4*e*	0	0	0.19408(9)	1.00	0.0053(5)
Ga5	2*b*	0	0	$\frac{1}{2}$	0.15(2)	0.007(4)
Ga6	16*n*	0	0.3732(9)	0.45563(16)	0.29(3)	0.0047(7)
$Ce_2Ag_{0.7(1)}Ga_{9.1(1)}$						
298 K						
Ce	4*e*	0	0	0.35251(2)	1.00	0.00865(19)
*M*1	4*d*(0.35(3)Ag+0.65(3)Ga)	0	$\frac{1}{2}$	$\frac{1}{4}$	1.00	0.0118(2)
Ga2	8*g*	0	$\frac{1}{2}$	0.9525(5)	0.19(4)	0.018(4)
Ga3	4*e*	0	0	0.09842(4)	1.00	0.0123(3)
Ga4	4*e*	0	0	0.19319(4)	1.00	0.0112(3)
Ga5	2*b*	0	0	$\frac{1}{2}$	0.06(3)	0.029(7)
Ga6	16*n*	0	0.3769(9)	0.45631(13)	0.37(3)	0.0185(9)
298 K						
Ce	4*e*	0	0	0.35253(3)	1.00	0.0053(3)
*M*1	4*d*(0.35(3)Ag+0.65(3)Ga)	0	$\frac{1}{2}$	$\frac{1}{4}$	1.00	0.0064(3)
Ga2	8*g*	0	$\frac{1}{2}$	0.9528(2)	0.19(4)	0.0059(10)
Ga3	4*e*	0	0	0.09831(5)	1.00	0.0067(4)
Ga4	4*e*	0	0	0.19312(5)	1.00	0.0065(3)
Ga5	2*b*	0	0	$\frac{1}{2}$	0.06(3)	0.008(6)
Ga6	16*n*	0	0.3709(5)	0.45618(7)	0.37(3)	0.0041(4)

[a] Occupancy.
[b] U_{eq} is defined at one third of the trace of the orthogonalized U_{ij} tensor.

with a beam to sample distance of 20 mm. Several aggregates of $La_2Ag_{1-x}Ga_{10-y}$ ($x\sim0.3$; $y\sim0.6$) and $Ce_2Ag_{1-x}Ga_{10-y}$ ($x\sim0.3$; $y\sim0.9$) were scanned at 10 different areas on the smooth surface of each aggregate. Several aggregates of $Ln_2Ag_{1-x}Ga_{10-y}$ (Ln=La, Ce) were scanned along the cross-section to investigate the formation a silver concentration gradient during crystal growth. The average compositions, standardized to Ln (Ln=La, Ce), are $La_2Ag_{0.67(5)}Ga_{9.17(13)}$ and $Ce_2Ag_{0.67(9)}Ga_{9.25(8)}$ and are consistent with refined compositions as obtained from single crystal X-ray diffraction. Measurement from two batches of $Ln_2Ag_{1-x}Ga_{10-y}$ (Ln=La, Ce) yielded the same concentrations within experimental error.

4. Physical property measurements

The temperature-dependent magnetic susceptibility, χ, of samples were measured from 3 to 265 K at H=0.1 T using a quantum design physical property measurement system (PPMS). At temperatures between 30 and 265 K, susceptibility data were fit using a modified Curie–Weiss equation. Field-dependent magnetization of the sample was measured from 0 to 5 T at 1.9 K and from 0 to 9 T at 3 K. Specific heat was measured using the thermal relaxation option of the PPMS down to 0.4 K. Temperature-dependent electrical resistance and magnetoresistance were measured using the four-probe method down to 3 K.

5. Results and discussion

5.1. Structure

$Ln_2Ag_{1-x}Ga_{10-y}$ (Ln=La, Ce) crystallize in the tetragonal $I4/mmm$ space group (No. 139) with crystallographic parameters provided in Table 1. The crystal structures of $Ln_2Ag_{1-x}Ga_{10-y}$ (Ln=La, Ce) can be viewed as disordered variants of Ce_2NiGa_{10} [32,39]. As shown in Fig. 1, the intergrowth of Ce_2NiGa_{10} (Fig. 1a) can be described as an inhomogeneous linear intergrowth of (Fig. 1b) $BaAl_4$-type $CeGa_4$ segments and (Fig. 1c) CaF_2-type $NiGa_2$ segments [39,40]. The $BaAl_4$-type segment, which is also a structural subunit in $YbGa_5$ [41], consists of layers of face-sharing tetragonal antiprisms $^2_\infty[Ce_{4/8}Ga_{4/4}]_2=CeGa_4$. Unlike $YbGa_5$, which has a $PtHg_2$-type segment [41], the CaF_2-type segment in Ce_2NiGa_{10} consists of face-sharing rectangular prisms $^2_\infty[Ga_{8/4}Ni]=Ga_2Ni$. Combination of the two segments yield $2CeGa_4$ (Fig. 1c)+Ga_2Ni (Fig. 1b)=Ce_2NiGa_{10} (Fig. 1a). In the case of $Ln_2Ag_{1-x}Ga_{10-y}$ (Ln=La, Ce) (Fig. 2a), the $BaAl_4$-type $Ce(Ag,Ga)_4$ segment (Fig. 2d) is built of layers of face-sharing tetragonal antiprisms $^2_\infty\left[Ce_{4/8}(Ag,Ga)_{4/4}\right]_2=CeAg_xGa_{4-x}$ with Ag ($\sim$40%) and Ga ($\sim$60%) mixing at the 4d ($-4m2$) site, and the distorted CaF_2-type gallium segment (Fig. 2c) consists of face-sharing cubes $^2_\infty[Ga_{8/4}Ga]=Ga_{3-y}$ with the center of the cubes partially occupied with 6–10% Ga. The combination of the two segments yields $2CeAg_xGa_{4-x}$ (Fig. 2d)+Ga_{3-y} (Fig. 2c)=$Ce_2Ag_{1-x}Ga_{10-y}$ (Fig. 2a).

Understanding the gallium network is critical for understanding the structure of $Ln_2Ag_{1-x}Ga_{10-y}$ (Ln=La, Ce). The disordered CaF_2-type gallium segments, shown in brackets 1–3 of Fig. 3, can be best visualized as the average of three structural units of the (Fig. 2b) $CeGa_6$-type segments. The disorder in this segment occurs around the site Ga5 (2b, 4/mmm) where Ga is substituted for Ni in the Ce_2NiGa_{10}. The Ga2 (8g) and Ga6 (16n) sites represent the vertices of a cube and are both partially occupied with short contacts ($\sim$2.4 Å) between the vertices and the center, Ga5 (2b), of the cube, see Fig. 2c. Similar gallium networks have been observed in the structurally related phases $YbGa_5$ (Ce_2NiGa_{10}-type structure) [41], $CeAg_xGa_{4-x}$ ($BaAl_4$-type structure) [20], $CeGa_6$ ($PuGa_6$-type structure) [42], and Ce_2NiGa_{10} (own-type structure). $YbGa_5$, like $Ln_2Ag_{1-x}Ga_{10-y}$ (Ln=La, Ce), is a disordered variant of Ce_2NiGa_{10}-structure type. In the distorted bicapped Ga cubes of $YbGa_5$, the authors suggested that the intrinsic disorder and split atom positions stem from the tendency of Ga to achieve the optimum coordination of four [41]. Previously published Ln:Ga (Ln=lanthanide) binary and Ln:Ag:Ga (Ln=lanthanide) ternary phases depict Ga in a four coordinate environment (with interatomic contacts between 2.5 and 2.6 Å) [20–32]. This includes Ga–Ga contacts as well as Ga–T (T=transition metal) contacts in these phases. In previously reported $YbGa_5$, a coordination of four can be obtained for all the

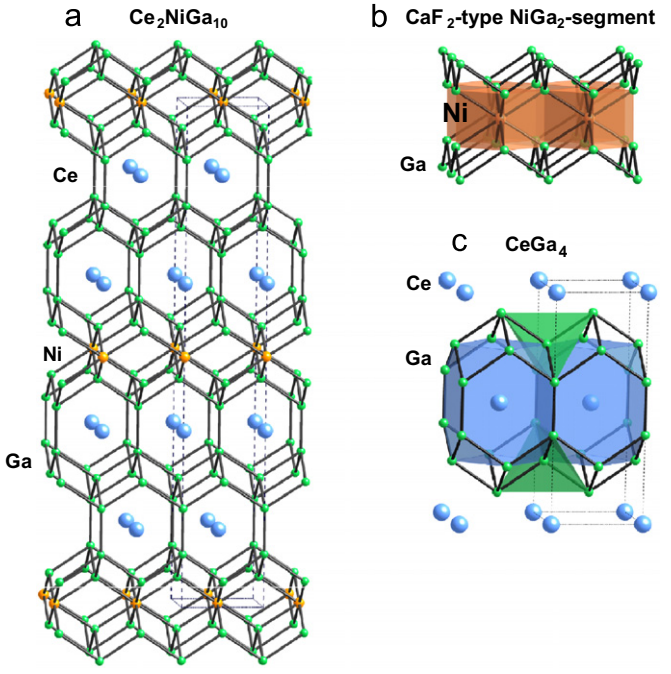

Fig. 1. (a) Ce_2NiGa_{10} is a linear intergrowth of (b) CaF_2-structure type $NiGa_2$-segments, and (c) $BaAl_4$-structure type $CeGa_4$ segments.

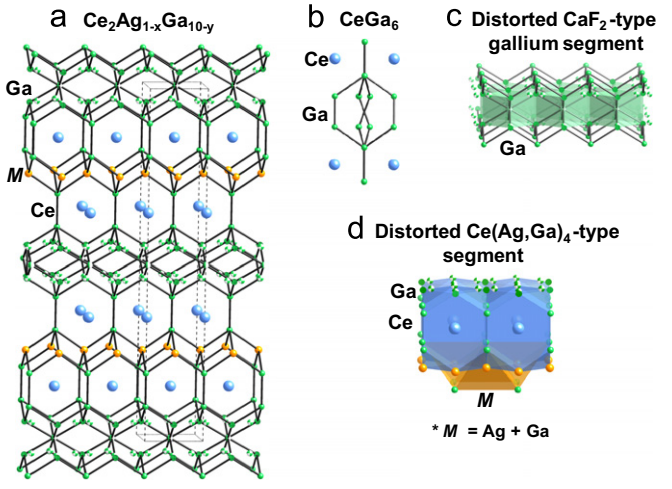

Fig. 2. (a) $Ce_2Ag_{0.7(1)}Ga_{9.1(1)}$ can be described as a distorted variant of the Ce_2NiGa_{10} structure with the (c) distorted gallium segments best described as variants of (b) $CeGa_6$ ($PuGa_6$-structure type). (d) The distorted $Ce(Ag,Ga)_4$-type segments are built of layers of face-sharing tetragonal antiprisms. Here M=Ag+Ga and the shaded atoms are partially occupied.

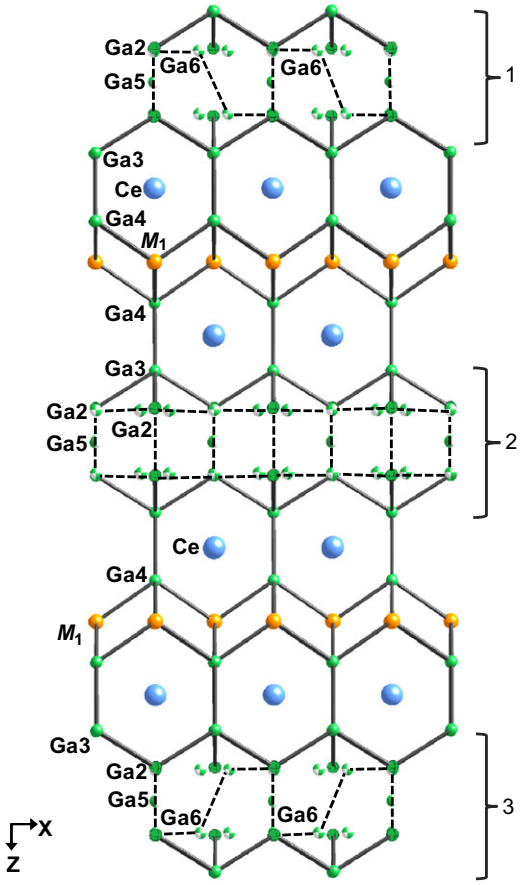

Fig. 3. The crystal structure of $Ce_2Ag_{0.7(1)}Ga_{9.1(1)}$ is shown here. The distorted CaF_2-type gallium segments are labeled in brackets 1–3. The dashed lines connecting hatched spheres represent likely bonds between disordered sites. These three segments, when superposed on each other, describes the average distorted CaF_2-type gallium segment of $Ce_2Ag_{1-x}Ga_{10-y}$. Segments 1 and 3 each represent ~40% of the average distorted CaF_2-type gallium segment and can be considered the majority components, whereas segment 2 represents ~20% of the average distorted CaF_2-type gallium segment and can be considered a minority component. The disorder in this structure can be rationalized from the tendency of Ga to be four coordinate. Here M=Ag+Ga and the shaded atoms are partially occupied.

Ga atoms by applying limits on interatomic distances found in previously published *Ln*:Ga (*Ln*=lanthanide) binary and *Ln*:Ag:Ga (*Ln*=lanthanide) ternary phases [20–32]. This approach results in the three most-likely components, shown in brackets 1–3 of Fig. 3, which when superposed on each other give the average crystal structure of $Ce_2Ag_{0.7(1)}Ga_{9.1(1)}$. The components in brackets 1 and 3 each represent ~40% of the total average structure and can be considered the majority components, whereas the component in bracket 2 represents ~20% of the average structure and can be considered the minority component. The Ga2 and Ga6 sites, which are positionally disordered, have a total occupancy of unity within experimental error. The dashed lines connecting hatched spheres in Fig. 3 represent likely bonds between disordered sites. *M*1 (*M*=Ag+Ga) is in the center of a tetrahedron of four Ga4 atoms. Ga3 is in the center of a tetrahedron of Ga4 and partially occupied Ga2 and Ga6 atoms. Ga4 is in the center of a distorted square pyramid with short contacts between Ga3 and Ga4 (~2.48 Å) and long contacts between *M* and Ga4 (~2.61 Å). The average Ga5-centered cube is shown in Fig. 2c.

The $YbGa_5$ structure is very similar to $Ln_2Ag_{1-x}Ga_{10-y}$ (*Ln*=La, Ce), yet there are two differences between $Ln_2Ag_{1-x}Ga_{10-y}$ (*Ln*=La, Ce) and $YbGa_5$. In $YbGa_5$, the symmetry of the compound is reduced with respect to the Ce_2NiGa_{10} parent structure due to a displacement of the Ga2 atom from the fourfold axis on the 4*mm* site, whereas in $Ln_2Ag_{1-x}Ga_{10-y}$ (*Ln*=La, Ce) the equivalent gallium site (4*mm*, 4*e*) remains on the fourfold axis. In $Ln_2Ag_{1-x}Ga_{10-y}$ (*Ln*=La, Ce), the Ga5 (4/*mmm*, 2*b*) site is partially occupied (~10%) whereas in $YbGa_5$ the 4/*mmm* (2*b*) site (the center of the cube) is vacant. The partial occupancy at the 4/*mmm* (2*b*) site in $Ln_2Ag_{1-x}Ga_{10-y}$ (*Ln*=La, Ce) coincides with a larger available volume of the disordered cube in which to accommodate a gallium atom compared to $YbGa_5$. $Ln_2Ag_{1-x}Ga_{10-y}$ (*Ln*=La, Ce) is not the first reported gallium-rich intermetallic phase with a distorted gallium network. Several gallium-rich intermetallic phases with a distorted gallium network include $LaNi_{1-x}Ga_6$ [39], $CeAg_{1.25}Ga_{4.25}$ [30], $YbGa_5$ [41], $Ln_5(Ag,Ga)_{19-x}$ (*Ln*=Gd, Tb; x~2.2) [29], ε-$SmGa_6$ [43], $Sm_2Ga_{1.8}Ge_{5.2}$ [44], $Sm_4Ga_{5.24}Ge_{5.76}$ [44] $Ca_3Au_{6.61}Ga_{4.39}$ [45], and $YbGa_{3.34}$ [46]. In addition to *Ln*:Ga (*Ln*=lanthanide) binary and Ln:Ag:Ga (*Ln*=lanthanide) ternary phases, complex GaGe-containing networks including YbGaGe

Table 3
Interatomic distances.

		298 K		100 K	
		$La_2Ag_{0.7(1)}Ga_{9.4(1)}$	$Ce_2Ag_{0.7(1)}Ga_{9.1(1)}$	$La_2Ag_{0.7(1)}Ga_{9.4(1)}$	$Ce_2Ag_{0.7(1)}Ga_{9.1(1)}$
		Distances (Å)			
Tetragonal antiprisms					
Ln–*M*1	(x4)	3.4507(7)	3.4320(5)	3.4423(10)	3.4235(5)
Ln–Ga2	(x4)	3.387(8)	3.380(10)	3.385(4)	3.378(4)
Ln–Ga3	(x4)	3.3181(7)	3.2951(6)	3.3089(11)	3.2847(6)
Ln–Ga4	(x4)	3.3019(7)	3.2618(6)	3.2913(10)	3.2501(6)
Ln–Ga5	(x1)	3.8569(8)	3.8530(6)	3.8467(13)	3.8453(6)
Ln–Ga6	(x4)	3.178(9)	3.158(4)	3.136(4)	3.134(2)
Tetrahedra *M**					
*M*1–*M*1	(x4)	3.0675(4)	3.0355(4)	3.0572(4)	3.0242(4)
*M*1–Ga4	(x4)	2.6157(8)	2.6095(7)	2.6085(14)	2.6024(8)
Gallium network					
Ga2–Ga2	(x1)	2.512(19)	2.48(2)	2.486(10)	2.49(3)
Ga2–Ga3	(x2)	2.547(5)	2.525(6)	2.542(3)	2.520(3)
Ga2–Ga5	(x2)	2.506(5)	2.479(6)	2.494(3)	2.467(3)
Ga2–Ga6	(x2)	0.519(8)	0.537(4)	0.555(4)	0.559(2)
Ga2–Ga6	(x2)	2.457(4)	2.440(8)	2.463(5)	2.6641(14)
Ga3–Ga4	(x1)	2.4870(19)	2.4759(15)	2.485(3)	2.4723(18)
Ga3–Ga6	(x8)	2.655(3)	2.6326(18)	2.646(3)	2.6260(12)

*M=Ag+Ga.

[10], $Ln_2MGa_9Ge_2$ (Ln=Ce, Sm; M=Ni, Co) [47], $Ln_3Ni_3Ga_8Ge_3$ (Ln=lanthanide) [48], $LnMGa_3Ge$ (Ln=lanthanide; M=Ni, Co) [6,7,48], and $Ln_4FeGa_{12-x}Ge_x$ (Ln=Sm, Tb; x=2.5) [49] have been the focus of recent work.

The disorder in the CaF_2-type gallium segment can be rationalized by the tendency of gallium to adopt a coordination of four. Analysis of the structures of $LaNi_{1-x}Ga_6$ [39], $CeAg_{1.25}Ga_{4.25}$ [30], $YbGa_5$ [41], $Ln_5(Ag,Ga)_{19-x}$ (Ln=Gd, Tb; $x\sim2.2$) [29], ε-$SmGa_6$ [43], and $YbGa_{3.34}$ [46] indicates that these disordered gallium networks can also be rationalized considering the tendency of gallium to be four coordinate. Select interatomic distances of $La_2Ag_{0.7(1)}Ga_{9.4(1)}$ and $Ce_2Ag_{0.7(1)}Ga_{9.1(1)}$ are provided in Table 3. The Ga–Ga and M–Ga (M=Ag+Ga) bond distances are $\sim$2.5 and $\sim$2.6 Å which are consistent with other AgGa-containing intermetallic compounds and with similar distorted gallium networks [20–32,38,41,46].

5.2. Physical properties

Previously reported $LnAg_xGa_{4-x}$ (Ln=La–Nd, Sm and Yb) with $0.3<x<0.7$ show property dependence on silver concentration [20,21], so measurements on $Ce_2Ag_{0.7(1)}Ga_{9.1(1)}$ were performed on multiple samples to determine the reproducibility of physical property measurements. No noticeable differences were observed, indicating that the range of silver concentration does not influence the physical properties in this phase.

Fig. 4 shows the resistance of $Ce_2Ag_{0.7(1)}Ga_{9.1(1)}$ down to 3 K. The slope of the resistance vs. temperature indicates metallic behavior with the low temperature region shown in the top-left inset. There is evidence of the decrease in spin disorder scattering near the magnetic ordering temperature as seen in the change in slope near 5 K. There is also a drop at 1.09 K attributable to the onset of superconductivity of gallium [50] due to surface Ga at the grain boundaries in the measured aggregate. The magneto-resistance of $Ce_2Ag_{0.7(1)}Ga_{9.1(1)}$, shown in the bottom-right inset, reaches 16% at 9 T.

The inverse magnetic susceptibility of $Ce_2Ag_{0.7(1)}Ga_{9.1(1)}$ at 0.1 T, shown in Fig. 5, is linear from 30 to 265 K, and the modified Curie–Weiss equation was used to fit χ from 30 to 265 K. The calculated effective moment of 2.49 μ_B is consistent with localized Ce^{3+} moments and the θ_W of $-17.3(9)$ indicates antiferromagnetic coupling between magnetic moments. A high-resolution measurement of a different sample clearly shows the onset of antiferromagnetic ordering below 3 K. Fig. 6 shows the field-dependent magnetization at 1.9 and 3 K. The field-dependent magnetization at 1.9 K is linear from -0.4 to 0.4 T, as seen in the top-left inset, which is indicative of antiferromagnetic ordering. The change in slope before -0.4 T and after 0.4 T can be attributed to a spin-flop transition. There is evidence of time-dependence which could possibly be due to spin glass-like behavior. As shown in the bottom-right inset, the temperature-normalized, field-dependent magnetization curves superpose, with the slight deviation due to measurement time differences. The magnetization of Ce^{3+} in $Ce_2Ag_{0.7(1)}Ga_{9.1(1)}$ is $\sim$0.82 μ_B at 5 T when measured at 1.9 K and $\sim$0.71 μ_B at 5 T when measured at 3 K. The $La_2Ag_{0.7(1)}Ga_{9.4(1)}$ exhibits metallic behavior with the magnetic susceptibility showing temperature independent paramagnetism down to 3 K.

Fig. 7 shows the specific heat, C_m/T, of $Ce_2Ag_{0.7(1)}Ga_{9.1(1)}$ as obtained by subtracting C_p/T of $La_2Ag_{0.7(1)}Ga_{9.4(1)}$. The inset shows the specific heat of both $Ce_2Ag_{0.7(1)}Ga_{9.1(1)}$ and $La_2Ag_{0.7(1)}Ga_{9.4(1)}$. The large peak at 3 K is consistent with the onset of antiferromagnetic ordering. The Sommerfeld parameter, γ, was determined experimentally by extrapolation to the y-intercept of C_m/T vs. T^2 from $C_m=\gamma T+\beta T^3$. The Sommerfeld parameter γ is $\sim$585 mJ/molCeK^2, fit from 6 to 11 K. The expected magnetic entropy (Rln2) for a Ce^{3+} atom is recovered under the transition. The Sommerfeld parameter for $La_2Ag_{0.7(1)}Ga_{9.4(1)}$ is $\sim$0.01 mJ/molLaK^2 and the Debye temperature is 204.3 K.

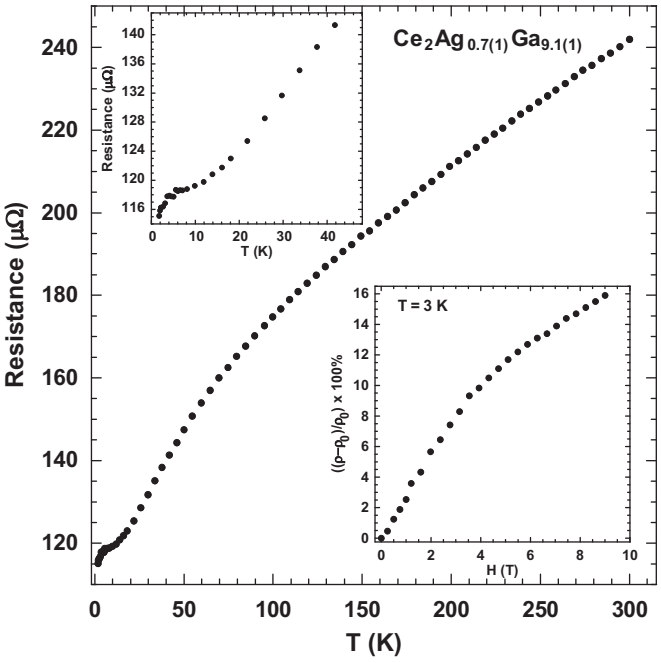

Fig. 4. The electrical resistance of $Ce_2Ag_{0.7(1)}Ga_{9.1(1)}$ is shown here at 0 T. The top-left inset shows an enhanced view of the low temperature electrical resistance. The bottom-right inset shows the magnetoresistance of $Ce_2Ag_{0.7(1)}Ga_{9.1(1)}$ at 3 K.

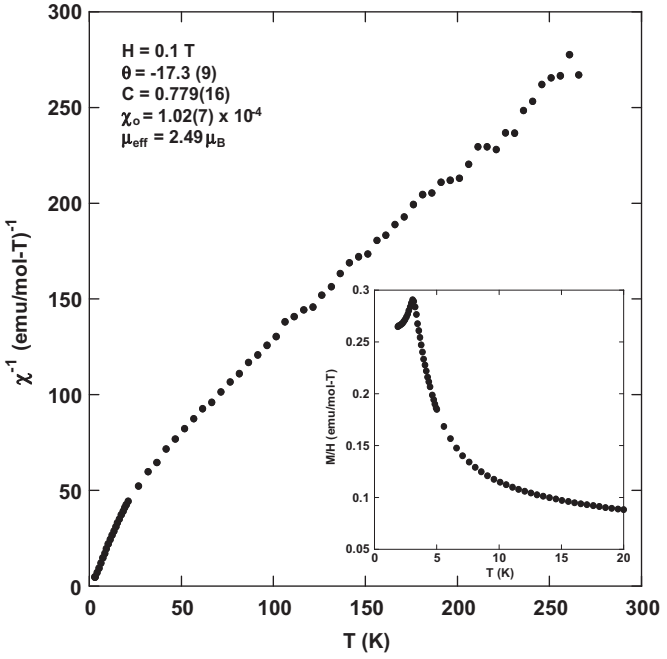

Fig. 5. The magnetic susceptibility of $Ce_2Ag_{0.7(1)}Ga_{9.1(1)}$ at 0.1 T is shown. The inverse magnetic susceptibility, shown in the inset, clearly indicates antiferromagnetism below 3 K. The inverse magnetic susceptibility plot is linear from 30 to 265 K and the modified Curie–Weiss equation was used to fit χ from 30 to 265 K.

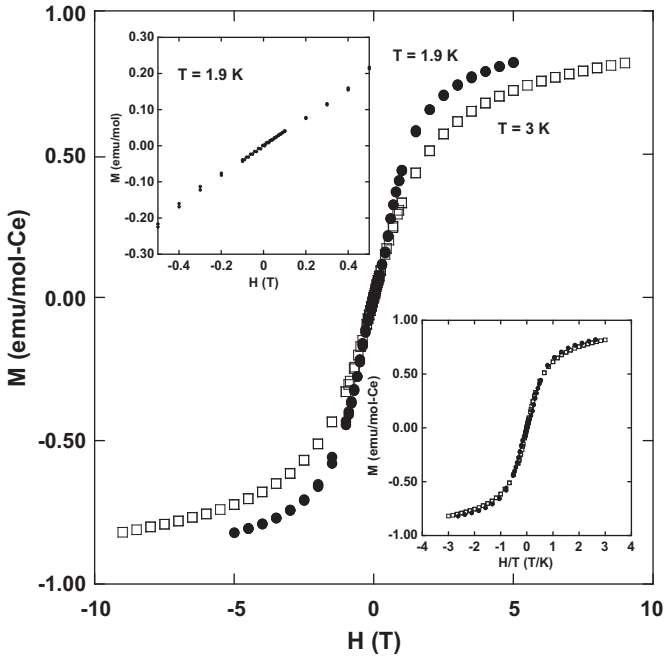

Fig. 6. The field-dependent magnetization of $Ce_2Ag_{0.7(1)}Ga_{9.1(1)}$ at 1.9 K from 0 to 5 T and at 3 K from 0 to 9 T. The field-dependent magnetization of $Ce_2Ag_{0.7(1)}Ga_{9.1(1)}$ at 1.9 K is linear from −0.4 to 0.4 T attributable to antiferromagnetic ordering. Above 0.4 T and below −0.4 T, there is a change in the slope attributable to a spin flop transition. As shown in the bottom-right inset, the temperature-normalized, field-dependent magnetization curves superpose on each other, with the slight deviation due to measurement time differences, which could possibly be attributable to spin glass-like behavior.

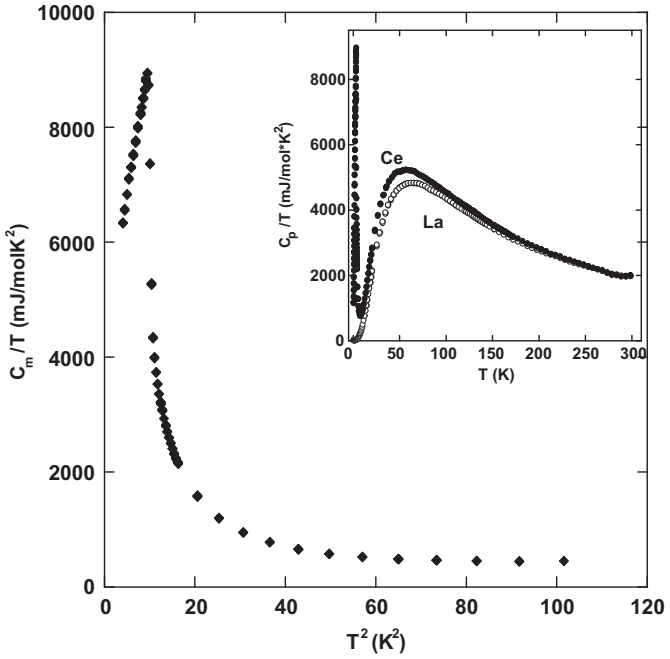

Fig. 7. The magnetic contribution to the heat capacity of $Ce_2Ag_{0.7(1)}Ga_{9.1(1)}$ is shown below 10 K. The large peak in C_m/T signals the onset of antiferromagnetic ordering. The inset shows the heat capacity of $Ln_2Ag_{1-x}Ga_{10-y}$ (Ln=La, Ce). The Sommerfeld parameter of $Ln_2Ag_{1-x}Ga_{10-y}$ (Ln=La, Ce) γ are ~0.01 mJ/molLaK^2 and ~585 mJ/molCeK^2, fit from 6 to 11 K.

5.3. Comparison between $Ce_2Ag_{0.7(1)}Ga_{9.1(1)}$ and $Ce(Ag,Ga)_4$

As $Ce_2Ag_{0.7(1)}Ga_{9.1(1)}$ is an intergrowth of gallium CaF_2-type segments and $Ce(Ag,Ga)_4$ segments, $Ce_2Ag_{0.7(1)}Ga_{9.1(1)}$ is compared to $Ce(Ag,Ga)_4$. The structural difference between $Ce_2Ag_{0.7(1)}Ga_{9.1(1)}$ and $Ce(Ag,Ga)_4$ is the extra gallium segment incorporated into the $Ce_2Ag_{0.7(1)}Ga_{9.1(1)}$. Both $Ce(Ag,Ga)_4$ and $Ce_2Ag_{0.7(1)}Ga_{9.1(1)}$ have approximately the same Ce–Ce interatomic distances along the *ab*-plane within experimental error with 4.308(7) Å in $Ce(Ag,Ga)_4$ to 4.293(6) Å in $Ce_2Ag_{0.7(1)}Ga_{9.1(1)}$. Although the extra layer of gallium increases the Ce–Ce next-nearest-neighbor interatomic distances along the *c*-axis from 10.784(10) Å in $Ce(Ag,Ga)_4$ to 13.410(13) Å in $Ce_2Ag_{0.7(1)}Ga_{9.1(1)}$, there is a small decrease in the Ce–Ce nearest-neighbor interatomic distances along the *c*-axis from 6.193(6) Å in $Ce(Ag,Ga)_4$ to 6.156(10) Å in $Ce_2Ag_{0.7(1)}Ga_{9.1(1)}$. The resistivity and resistance curves of $Ce(Ag,Ga)_4$ and $Ce_2Ag_{0.7(1)}Ga_{9.1(1)}$ exhibit the same shape indicating metallic behavior, and both $Ce(Ag,Ga)_4$ and $Ce_2Ag_{0.7(1)}Ga_{9.1(1)}$ exhibit a broad shoulder below 150 and 125 K, respectively, and a reminiscent-Kondo-like turn at low temperature [14,33,34]. The broad shoulder can be attributable to Kondo spin compensation. The magnetoresistance of $Ce_2Ag_{0.7(1)}Ga_{9.1(1)}$ is positive (~16% at 9 T), whereas $Ce(Ag,Ga)_4$ shows negative magnetoresistance (−2%) at 6 T for both 4 and 10 K measurements due to a weakened Kondo effect [33]. The field-dependent magnetization of $Ce(Ag,Ga)_4$ exhibits hysteresis from −0.1 to 0.1 T and saturation between 0.7 and 0.8 μ_β near 8 T [14,33], whereas the field-dependent magnetization of $Ce_2Ag_{0.7(1)}Ga_{9.1(1)}$ is linear from −0.4 to 0.4 T attributable to antiferromagnetic ordering. Both $Ce_2Ag_{0.7(1)}Ga_{9.1(1)}$ and $Ce(Ag,Ga)_4$ order at 3 K [14,33,34], as indicated in the magnetic susceptibility and in the heat capacity for both $Ce(Ag,Ga)_4$ and $Ce_2Ag_{0.7(1)}Ga_{9.1(1)}$. The effect of the extra gallium layer is evident in the change in magnetic ordering from ferromagnetic in $Ce(Ag,Ga)_4$ to antiferromagnetic in $Ce_2Ag_{0.7(1)}Ga_{9.1(1)}$. It is clear that the effect of the extra gallium layer on magnetic ordering is not a simple extrapolation due to the addition of conduction electrons.

6. Conclusion

$La_2Ag_{0.7(1)}Ga_{9.4(1)}$ and $Ce_2Ag_{0.7(1)}Ga_{9.1(1)}$ phases were grown as part of our investigations of crystal structure on physical properties. The tendency for split sites and partial occupancy follows from the coordination preference of Ga [41]. The Ag atoms occupy a different crystallographic site in $Ce_2Ag_{0.7(1)}Ga_{9.1(1)}$ than Ce_2MGa_{10} (M=Ni, Pd) [11,32]. In $Ce_2Ag_{0.7(1)}Ga_{9.1(1)}$, the Ag atoms share the 4*d* (−4*m*2) site with Ga, which is the equivalent site of mixing in $Ce(Ag,Ga)_4$. As a result of comparing $Ce_2Ag_{0.7(1)}Ga_{9.1(1)}$ and $Ce(Ag,Ga)_4$, although the structurally similar, magnetic behavior is different.

Acknowledgments

M.C.M. would like to acknowledge Dr. Jung Young Cho for useful discussions and NSF DMR-0756281 for support of this project. P.W.A. acknowledges the support of the DOE under Grant no. DE-FG02-07ER46420. D.P.Y. would like to acknowledge the support of the NSF under Grant no. DMR-0449022.

Appendix A. Supporting materials

Supplementary data associated with this article can be found in the online version at doi:10.1016/j.jssc.2010.06.011.

References

[1] J.L. Sarrao, L.A. Morales, J.D. Thompson, B.L. Scott, G.R. Stewart, F. Wastin, J. Rebizant, P. Boulet, E. Colineau, G.H. Lander, Nature 420 (2002) 297.

[2] N.J. Curro, T. Caldwell, E.D. Bauer, L.A. Morales, M.J. Graf, Y. Bang, A.V. Balatsky, J.D. Thompson, J.L. Sarrao, Nature 434 (2005) 622.
[3] I. Opahle, P.M. Oppeneer, Phys. Rev. Lett. 15 (2003) 90.
[4] J.Y. Cho, M. Moldovan, D.P. Young, J.Y. Chan, J. Phys.: Condens. Matter 19 (2007) 266224.
[5] R.T. Macaluso, S. Nakatsuji, H. Lee, Z. Fisk, M. Moldovan, D.P. Young, J.Y. Chan, J. Solid State Chem. 174 (2003) 296.
[6] D.L. Gray, M.C. Francisco, M.G. Kanatzidis, Inorg. Chem. 47 (2008) 7243.
[7] M.A. Zhuravleva, M. Evain, V. Petricek, M.G. Kanatzidis, J. Am. Chem. Soc. 129 (2007) 3082.
[8] R. Troc, P. Rogl, V.H. Tran, A. Czopnik, J. Solid State Chem. 158 (2001) 227.
[9] J.R. Salvador, F. Guo, T. Hogan, M.G. Kanatzidis, Nature 425 (2003).
[10] S. Margadonna, L. Prassides, A.N. Fitch, J.R. Salvador, M.G. Kanatzidis, J. Am. Chem. Soc. 126 (2004) 4498.
[11] J.N. Millican, R.T. Macaluso, D.P. Young, M. Moldovan, J.Y. Chan, J. Solid State Chem. 177 (2004) 4695.
[12] R.T. Macaluso, J.N. Millican, S. Nakatsuji, H.-O. Lee, B. Carter, N.O. Moreno, Z. Fisk, J.Y. Chan, J. Solid State Chem. 178 (2005) 3547.
[13] J.Y. Cho, J.N. Millican, C. Capan, D.A. Sokolov, M. Moldovan, A.B. Karki, D.P. Young, M.C. Aronson, J.Y. Chan, Chem. Mater. 20 (2008) 6116.
[14] J.Y. Cho, M. Moldovan, D.P. Young, N.D. Lowhorn, J.Y. Chan, Physica B 403 (2008) 795.
[15] J.Y. Cho, E.L. Thomas, Y. Nambu, C. Capan, A.B. Karki, D.P. Young, K. Kuga, S. Nakatsuji, J.Y. Chan, Chem. Mater. 21 (2009) 3072.
[16] K.R. Thomas, J.Y. Cho, J.N. Millican, R.D. Humbree, M. Moldovan, A. Karki, D.P. Young, J.Y. Chan, J. Cryst. Growth . doi:10.1016/j.jcrysgro.2009.12.039.
[17] H. Hegger, C. Petrovic, E.G. Moshopoulou, M.F. Hundley, J.L. Sarrao, Z. Fisk, J.D. Thompson, Phys. Rev. Lett. 84 (2000) 4986.
[18] C. Petrovic, R. Movshovich, M. Jaime, P.G. Pagliuso, M.F. Hundley, J.L. Sarrao, Z. Fisk, J.D. Thompson, Europhys. Lett. 53 (2001) 354.
[19] C. Petrovic, P.G. Pagliuso, M.F. Hundley, R. Movshovich, J.L. Sarrao, J.D. Thompson, Z. Fisk, P. Monthoux, J. Phys. Condens. Matter 13 (2001) L337.
[20] Y. Grin, K. Hiebl, P. Rogl, R. Eibler, J. Less-Common Met. 115 (1986) 367.
[21] Y. Grin, M. Ellner, K. Heibel, P. Rogl, J. Alloys Compd. 196 (1993) 207.
[22] Y. Grin, M. Ellner, K. Hiebl, P. Rogl, O.M. Sichevich, O.M. Myakush, J. Solid State Chem. 105 (1993) 399.
[23] T. Krachan, B. Stel'makhovych, Y. Kuz'ma, J. Alloys Compd. 386 (2005) 147.
[24] Y. Grin, M. Ellner, K. Hiebl, B. Baumgartner, P. Rogl, J. Alloys Compd. 221 (1995) 125.
[25] R.V. Gumeniuk, I.B. Taras, Y.B. Kuzma, J. Alloys Compd. 416 (2006) 131.
[26] A. Zygmunt, A. Szytula, M. Kolenda, Z. Tomkowicz, N. Stüsser, J. Leciejewicz, J. Magn. Magn. Mater. 161 (1996) 127.
[27] D. Rossi, D. Macciò, J. Alloys Compd. 281 (1998) 222.
[28] D. Rossi, R. Ferro, J. Alloys Compd. 317-318 (2001) 521.
[29] R.V. Gumeniuk, L.G. Akselrud, Y.B. Kuz'ma, Z. Naturforsch. B: Chem. Sci. 60 (2005) 929.
[30] R.V. Gumeniuk, L.G. Akselrud, B. Stel'makhovych, Y.B. Kuzma, J. Alloys Compd. 389 (2005) 127.
[31] R.V. Gumeniuk, Y. Prots, W. Schnelle, U. Burkhardt, Y.B. Kuzma, Y.N. Grin, J. Alloys Compd. 469 (2009) 28.
[32] Y.P. Yarmolyuk, Y.N. Grin, I.V. Rozhdestvenskaya, O.A. Usov, A.M. Kuzmin, V.A. Bruskov, E.I. Gladyshevskij, Kristallografiya 27 (1982) 599.
[33] I. Das, E.V. Sampathkumaran, Phys. Rev. B: Condens. Matter 48 (1993) 16103.
[34] H. Flandorfer, P. Rogl, E. Bauer, H. Michor, R. Hatzl, E. Gratz, C. Godart, J. Phys. Condens. Matter 8 (1996) 2365.
[35] A. Altomare, M.C. Burla, M. Camalli, G. Cascarano, C. Giacovazzo, A. Guagliardi, G. Polidori, J. Appl. Crystallogr. 27 (1994) 435.
[36] G.M. Sheldrick, Acta Crystallogr. A. A64 (2008) 112.
[37] A.L. Spek, J. Appl. Crystallogr. 36 (2003) 7.
[38] R.V. Gumeniuk, B. Stel'makhovych, Y.B. Kuzma, J. Alloys Compd. 352 (2003) 128.
[39] Y. Grin, Y.P. Yarmolyuk, E.I. Gladyshevskii, Sov. Phys. Crystallogr. 27 (1982) 413.
[40] E. Parthe, Modern Perspectives in Inorganic Chemistry, 382, Kluwer Academic Publishers, Boston, 1992 p 77–95.
[41] R. Giedigkeit, R. Niewa, W. Schnelle, Y. Grin, R. Kniep, Z. Anorg. Allg. Chem. 628 (2002) 1692.
[42] Pelleg, J. Less-Common Met. 81 (1981) 33.
[43] M. Tillard, D. Zitoun, C. Belin, Inorg. Chem. 48 (2009) 2399.
[44] Y.O. Tokaychuk, Y.E. Filinchuk, A.O. Fedorchuk, A.Y. Kozlov, I.R. Mokra, J. Solid State Chem. 179 (2006).
[45] D. Kubmann, R.D. Hoffman, R. Pottgen, Z. Anorg. Allg. Chem 627 (2001) 2053.
[46] M. Tillard, C. Belin, Inorg. Chem. 48 (2009) 9250.
[47] M.A. Zhuravleva, M.G. Kanatzidis, Inorg. Chem. 47 (2008) 9471.
[48] M.A. Zhuravleva, R.J. Pcionek, X. Wang, A.J. Schultz, M.G. Kanatzidis, Inorg. Chem. 42 (2003) 6412.
[49] M.A. Zhuravleva, X. Wang, A.J. Schultz, T. Bakas, M.G. Kanatzidis, Inorg. Chem. 41 (2002) 6056.
[50] C. Kittel, Introduction to Solid State Physics, 7th ed., John Wiley & Sons, Inc., New York, 1996.